Inorg. Chem. **2003**, *42*, 2751–2758

Inorganic Chemistry
Article

A Density Functional Evaluation of an Fe(III)–Fe(IV) Model Diiron Cluster: Comparisons with Ribonucleotide Reductase Intermediate X

Wen-Ge Han,* Timothy Lovell,* Tiqing Liu, and Louis Noodleman*

Department of Molecular Biology, TPC15, The Scripps Research Institute,
10550 N. Torrey Pines Rd., La Jolla, California 92037

Received July 19, 2002

Using broken-symmetry density functional theory and spin-projection methods, we have examined the electronic structure and properties of a large mixed-valent Fe(III)–Fe(IV) diiron system that displays two bidentate carboxylates and a single μ-oxo moiety as bridging ligands. Two carboxylates and a single oxygen species have long been implicated as core elements of the elusive intermediate X in ribonucleotide reductase. Spectroscopic studies of X have also identified the presence of an additional terminal or bridging oxygen-based ligand. Introduction of a second oxygen and protonated variants thereof in the core of our structural model is favored as a bridging hydroxide based on the lowest energy structure. Mössbauer measurements indicate clearly that the two iron sites of X are distinct and that there is significant electron delocalization onto the oxygen-based ligands. For several examined spin states of our model cluster, Mössbauer parameters from density functional calculations are neither able to differentiate between the iron sites nor reproduce the strong spin delocalization onto the oxygen-based ligands observed experimentally. The combined comparison of the calculated geometries, spin states, spin densities, and Mössbauer properties for our model clusters with available experimental data for X implies that intermediate X is significantly different from the diiron structural models examined herein.

1. Introduction

Ribonucleotide reductase (RNR) catalyzes the reduction of ribonucleotides to deoxyribonucleotides.[1,2] This is the first step in the required biosynthesis of DNA. Though different classes of this enzyme differ in composition and cofactor requirements, they display a reaction mechanism with a common theme using metals and free radical chemistry. The class I RNRs consist of a homodimer of two dissimilar protein subunits, R1 and R2, in an overall $\alpha_2\beta_2$ tetramer. Subunit R1 contains the substrate binding site, and R2 contains one binuclear iron cluster which generates and stabilizes a radical at tyrosine 122 (Tyr122). This radical functions as a "pilot light" which begins the catalytic reaction via long-range proton-coupled electron transfer to generate a thiyl radical on cysteine 439 (Cys439) of the R1 subunit, which then performs the ribonucleotide reduction.[3,4] The Tyr122 radical has been identified in the oxidized deprotonated form and is stable for days at room temperature.[1] Once the Tyr122 radical is lost, the enzyme becomes inactive, but the active form can be regenerated by adding O_2 plus ferrous iron and reductant to the apo-R2 enzyme. The overall net reaction is given by

$$\text{Tyr122-OH} + 2\text{Fe(II)} + O_2 + e^- + H^+ \rightarrow \text{Tyr122-O}^\bullet + \text{Fe(III)}-\text{O}-\text{Fe(III)} + H_2O \quad \text{(I)}$$

Presently, the structure for the active form of the protein that contains the Tyr122 radical is unknown, but X-ray structures of RNR from *Escherichia coli* are available for both the reduced and oxidized (met) forms (see Figure 1).[5−8]

During the formation (reaction I) of active R2, a transient species (intermediate X) is formed that oxidizes tyrosine to the stable radical form.[9−12] Though there has been a

---

* To whom correspondence should be addressed. E-mail: wengehan@scripps.edu; tlovell@scripps.edu; lou@scripps.edu. Fax: 858-7848896.

(1) Wallar, B. J.; Lipscomb, J. D. *Chem. Rev.* **1996**, *96*, 2625−2657.
(2) Sjöberg, B. M. *Struct. Bond* **1997**, *88*, 139−173.
(3) Sturgeon, B. E.; Burdi, D.; Chen, S.; Huynh, B. H.; Edmondson, D. E.; Stubbe, J.; Hoffman, B. M. *J. Am. Chem. Soc.* **1996**, *118*, 7551−7557.
(4) Stubbe, J.; van der Donk, W. A. *Chem. Biol.* **1995**, *2*, 793−801.
(5) Nordlund, P.; Sjoberg, B. M.; Eklund, H. *Nature* **1990**, *345*, 593−598.
(6) Nordlund, P.; Eklund, H. *J. Mol. Biol.* **1993**, *232*, 123−164.
(7) Nordlund, P.; Eklund, H. *Curr. Opin. Struct. Biol.* **1995**, *5*, 758−766.
(8) Logan, D. T.; Su, X. D.; Åberg, A.; Regnström, K.; Hajdu, J.; Eklund, H.; Nordlund, P. *Structure* **1996**, *4*, 1053−1064.

10.1021/ic020465l CCC: $25.00

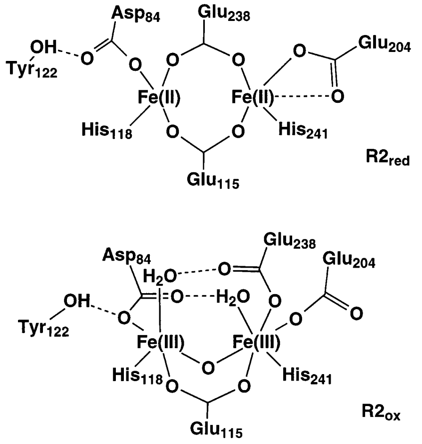

Figure 1. Core structures of diferrous[8] ($R2_{red}$) and diferric[6] ($R2_{ox}$(met)) RNR-R2 from *E. coli*.

significant experimental attempt to elucidate the structure of this short-lived catalytic species, the detailed structure of intermediate X is still not clear.[3,9,10,13−17] The accumulated experimental evidence now enables a reasonable picture of X to be established. Mössbauer data indicate the iron centers of X are high-spin Fe(III) ($S = 5/2$) and high-spin Fe(IV) ($S = 2$) sites that antiferromagnetically couple to give an $S_{total} = 1/2$ ground state.[3] X is therefore best described as a spin-coupled Fe(III)−O−Fe(IV) system that displays no Tyr122 radical. A short Fe−Fe distance of 2.5 Å has been identified by EXAFS for X in both wild-type and mutant Y122F proteins.[16] On the basis of this metric, possible core structures for X have been proposed and these are shown in Figure 2.[16,18] Experimental data support the existence of at least one μ-oxo bridge in the core structure of X, but beyond this, other elements that may be present include terminal or bridging solvent-based ligands and monodentate and/or bidentate bridging carboxylate groups from glutamate (Glu) protein residues. Recently, on the basis of CW and pulsed Q-band ^{17}O-ENDOR experiments, as well as ENDOR[15] and EXAFS[16] observations, Burdi et al.[17] proposed a structure for X, containing two oxygen atoms, both initially derived from O_2, with one present as a μ-oxo bridge and one as a terminal aqua ligand.

In contrast to the wealth of experimental studies, few theoretical studies have focused on the structure and spin states of the RNR active site.[19−21] One model of intermediate X has been examined in detail by Siegbahn,[19] which contains (see Figure 6 in ref 19) one μ-oxo bridge, one hydroxo bridge, and two bidentate carboxylates from Glu115 and Glu238. Following geometry optimization of this $S_{total} = 1/2$ model using the B3LYP density functional theory (DFT) approach,[19] an Fe−Fe distance of 2.61 Å was obtained. Furthermore, spin populations of 0.99 and −1.71 were noted for the two iron sites. Such small spin populations are more characteristic of low-spin and intermediate-spin Fe centers rather than high-spin Fe sites and appear inconsistent with the Mössbauer data for X.

In this paper, we reexamine the model for intermediate X with two bidentate carboxylates and one μ-oxo bridge. On the basis of the proposal of Burdi et al.,[17] we also evaluate whether an additional oxygen ligand can be present as a terminal or bridging H_2O or hydroxide. To incorporate second-shell hydrogen bonding as well as possible charge-transfer effects to the cluster, we have surrounded the cluster model by second- and third-shell H-bonding partners similar to those found in the RNR protein environment for the resting and reduced oxidation states. These protein residues are also assumed to be present for intermediate X. This allows us to examine whether the irons are present as high-spin or intermediate-spin sites in a much larger quantum mechanical description of the protein environment and whether the ground state of the cluster model has total spin $S_{total} = 1/2$. Finally, by comparing the calculated and observed Mössbauer data, we evaluate the relationship of this model to that of intermediate X in RNR.

2. Active Site Cluster Models

For our initial calculations, we made use of a small model cluster which includes first-shell ligands that are derived from the amino acid side chains found in the protein environment of RNR for the oxidized and reduced states. These side chains are aspartate 84 (Asp84), histidine 118 (His118), Glu115, His241, Glu204, and Glu238 (see labels in Figure 3a). Since a μ-oxo bridge lies between His118 and His241 in the active site of $R2_{ox}$, we also maintain this position for the μ-oxo bridge (O1 in Figure 3). The additional oxygen (O2) is on the opposite side of the cluster model and lies between Asp84 and Glu204. The initial positions of the first shell ligands were taken from chain A of the oxidized RNR X-ray crystal structure (PDB code: 1RIB).[6] The orientation of the carboxylate group of the Glu238 side chain was rearranged similar to that in the reduced RNR structure (PDB code: 1XIK),[8] in order to obtain a bidentate bridging coordination. The hydrogen atoms were added to the crystal structure using InsightII.[22] To allow intermediate X to accumulate and facilitate spectroscopic characterization of X, the majority of experiments have been performed on a

---

(9) Bollinger, J. M., Jr.; Edmondson, D. E.; Huynh, B. H.; Filley, J.; Norton, J. R.; Stubbe, J. *Science* **1991**, *253*, 292−298.

(10) Bollinger, J. M., Jr.; Stubbe, J.; Huynh, B. H.; Edmondson, D. E. *J. Am. Chem. Soc.* **1991**, *113*, 6289−6291.

(11) Ravi, N.; Bollinger, J. M., Jr.; Huynh, B. H.; Edmondson, D. E.; Stubbe, J. *J. Am. Chem. Soc.* **1994**, *116*, 8007−8014.

(12) Bollinger, J. M., Jr.; Tong, W. H.; Ravi, N.; Huynh, B. H.; Edmondson, D. E.; Stubbe, J. *J. Am. Chem. Soc.* **1994**, *116*, 8015−8023; *116*, 8024−8032.

(13) Burdi, D.; Sturgeon, B. E.; Tong, W. H.; Stubbe, J.; Hoffman, B. M. *J. Am. Chem. Soc.* **1996**, *118*, 281−282.

(14) Veselov, A.; Scholes, C. P. *Inorg. Chem.* **1996**, *35*, 3702−3705.

(15) Willems, J. P.; Lee, H. I.; Burdi, D.; Doan, P. E.; Stubbe, J.; Hoffman, B. M. *J. Am. Chem. Soc.* **1997**, *119*, 9816−9824.

(16) Riggs-Gelasco, P. J.; Shu, L.; Chen, S.; Burdi, D.; Huynh, B. H.; Que, Jr. L.; Stubbe, J. *J. Am. Chem. Soc.* **1998**, *120*, 849−860.

(17) Burdi, D.; Willems, J. P.; Riggs-Gelasco, P. J.; Antholine, W. E.; Stubbe, J.; Hoffman, B. M. *J. Am. Chem. Soc.* **1998**, *120*, 12910−12919.

(18) Hsu, H. F.; Dong, Y.; Shu, L.; Young, Jr. V. G.; Que, L., Jr. *J. Am. Chem. Soc.* **1999**, *121*, 5230−5237.

(19) Siegbahn, P. E. M. *Inorg. Chem.* **1999**, *38*, 2880−2889.

(20) Siegbahn, P. E. M.; Eriksson, L.; Himo, F.; Pavlov, M. *J. Phys. Chem. B* **1998**, *102*, 10622−10629.

(21) Lovell, T.; Li, J.; Noodleman, L. *J. Biol. Inorg. Chem.* **2002**, *7*, 799−809.

(22) *Insight II User Guide*; San Diego, CA, 1995.

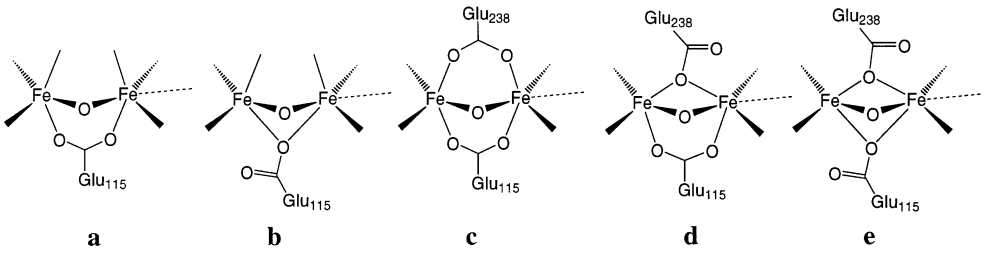

Figure 2. Possible core structures of intermediate X proposed previously based on recent experimental observations.[15−18] The two carboxylates from Glu115 and Glu238 are monodentately or bidentately binding to the diiron centers. One of the oxygen atoms derived initially from O_2 is present as a μ-oxo bridge. There are additional oxygen type ligands (OH_n), either bridging or terminal.

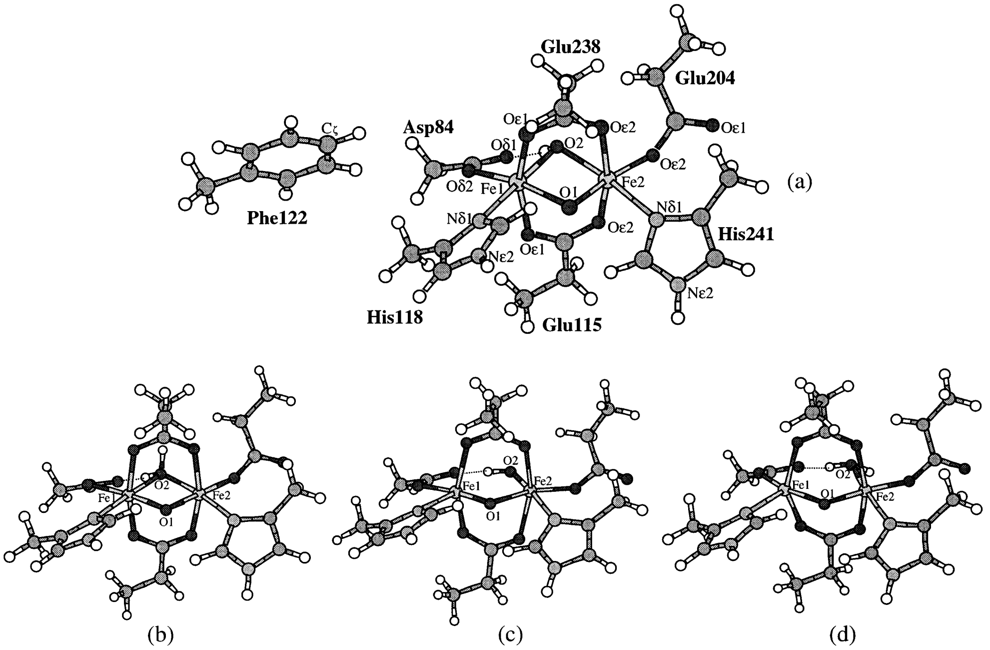

Figure 3. Small quantum cluster models of (a) $(OH^-)_{br}$ with a bridging hydroxide, (b) $(H_2O)_{br}$ with a bridging H_2O, (c) $(OH^-)_t$ with a terminal hydroxide, and (d) $(H_2O)_t$ with a terminal H_2O. All models have two bidentate carboxylate groups and a μ-oxo bridge. The side chain of Phe122 is not shown in (b)−(d) but is included in each model during the calculations.

R2 mutant (Y122F), in which Tyr122 is replaced by a nonoxidizable amino acid phenylalanine 122 (Phe122).[3,9,10,13−17] For consistency with the mutagenesis experiments, we have replaced Tyr122 with Phe122 in the $R2_{ox}$ structure and incorporated the Phe122 side chain into our active site model.

To evaluate the most likely location and protonation state of a second oxygen species introduced into our structural model, four structural models are examined that contain the following: bridging hydroxide (see Figure 3a); bridging H_2O (Figure 3b); terminal hydroxide (Figure 3c); terminal H_2O (Figure 3d). We will find subsequently in the results section that, on the basis of energy and pK_a criteria, the preferred model displays a bridging hydroxide.

The size of this preferred smaller model has been expanded to a much larger model that incorporates second- and third-shell ligands to examine the influence that H-bonding and charge transfer has on several possible spin coupled states which satisfy the $S_{total} = 1/2$ spin criterion of the cluster. These additional residues are extracted from the protein environment and include tryptophan 111 (Trp111) and 48 (Trp48), glutamine 43 (Gln43), serine 114 (Ser114), Asp237, and a water molecule (HOH621) as it appears in $R2_{ox}$ (see Figure 4).[6] The H-bonding interactions that result are the following: Trp111-$N_{\epsilon 1}$H···$O_{\epsilon 2}$-Glu204; HOH621···$O_{\epsilon 1}$-Glu204; Gln43-$O_{\epsilon 1}$···H$N_{\epsilon 2}$-His241; Ser114-O_{γ}···H$N_{\epsilon 2}$-His241; Asp237-$O_{\delta 2}$···H$N_{\epsilon 2}$-His118; Asp237-$O_{\delta 2}$···H$N_{\epsilon 1}$-Trp48; Asp237-$O_{\delta 1}$···H$N_{\epsilon 2}$-Gln43. Upon reaction of O_2 with the reduced Fe(II)−Fe(II) cluster to form intermediate X, an electron has to be transferred to one of the Fe centers to create the Fe(III)−Fe(IV) state. It has been proposed that this electron originates from Trp48, which lies close to the surface of the R2 protein, and subsequently, Trp48 obtains an electron back from the environment.[1,23] We therefore also included the Trp48 side chain, which also has a H-bonding interaction with Asp237 (see Figure 4), into our large model. Both Trp48 and Trp111 side chains are assigned neutral charge in our current calculations.

All side chain ligands for both the small and larger models were extracted from the protein coordinates (PDB: 1RIB) by breaking the $C_\beta-C_\alpha$ bond. To fill the open valence of atom C_β, a linking hydrogen atom[24] was added along the $C_\beta-C_\alpha$ vector (with bond length of 1.106 Å for $C_\beta-H_{link}$).

---

(23) Krebs, C.; Chen, S.; Baldwin, J.; Ley, B. A.; Patel, U.; Edmondson, D. E.; Huynh, B. H.; Bollinger, J. M., Jr. *J. Am. Chem. Soc.* **2000**, *122*, 12207−12219.

(24) Han, W.-G.; Tajkhorshid, E.; Suhai, S. *J. Biol. Struct. Dyn.* **1999**, *16*, 1019−1032.

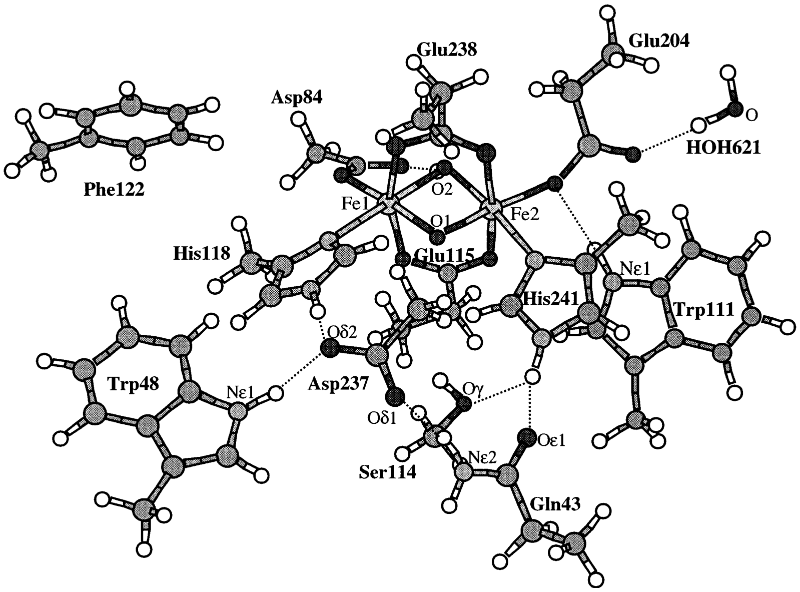

Figure 4. Larger quantum cluster model of $(OH^-)_{br}$ with a bridging hydroxide.

The $H_{linking}$ atom positions, except those in Glu238, Asp84, and Phe122, are fixed during geometry optimizations.

3. Computational Methodology

3.1. DFT Calculations. All DFT calculations have been performed using the Amsterdam Density Functional (ADF, version 2.3) package.[25-28] The parametrization of Vosko, Wilk, and Nusair (VWN)[29] was used for the local density approximation term, and the corrections of Perdew and Wang (PW91)[30] were used for the nonlocal exchange and correlation terms. Basis set IV was applied for the two iron sites (uncontracted triple-ζ Slater-type orbitals (STO) for the 3s, 3p, 3d, and 4s valence orbitals along with a 4p polarization orbital) and basis set III for all other atoms (double-ζ STOs for 2s, 2p valence orbitals of C, N, O augmented with a 3d polarization orbital, and double-ζ STO for 1s of H with a 2p polarization orbital). The inner core shells of C(1s), N(1s), O(1s), and Fe(1s, 2s, 2p) were treated by the frozen core approximation. The accuracy parameter (accint) for the numerical integration grid was set to 4.0 and 3.5 for small and large model calculations, respectively. The spin-unrestricted method was used for all density functional calculations.

3.2. Broken-Symmetry and Spin Projection. Experimentally, X is known to adopt an Fe(III)−Fe(IV) $S_{total} = 1/2$ ground state, and the two Fe sites are high spin and antiferromagnetically (AF) coupled.[3] This implies AF coupling of site spins $S_A = 5/2$ and $S_B = 2$ (A = Fe(III), B = Fe(IV)). Considering that there are intermediate spin alignments, i.e., $\{S_A = 3/2, S_B = 2\}$, $\{S_A = 3/2, S_B = 1\}$, $\{S_A = 1/2, S_B = 1\}$, and $\{S_A = 1/2, S_B = 0\}$, which also produce $S_{total} = |S_A - S_B| = 1/2$, we also performed the intermediate AF and ferromagnetic (F) geometry optimization and energy calculations on the large models with a hydroxide bridge (Figure 4).

Usually, the AF spin-coupled state cannot be obtained directly from the normal DFT calculations in ADF. As in previous work, we represent the AF spin-coupled state in DFT by a “broken-symmetry” state, where a spin-unrestricted determinant is constructed in which one of the Fe sites displays spin-up electrons in the majority and the other site has spin-down electrons.[31-35] The energy for the pure spin state is then be calculated via spin projection (decontamination).[31-35] To obtain this broken-symmetry solution, one has to first construct an F-spin-coupled ($S_{total} = S_{max} = S_A + S_B$) determinant, where the spins on both irons are aligned in a parallel fashion. Then, we rotate the spin vector located on either atom Fe1 or atom Fe2 by interchanging the α and β fit densities for that Fe site from the output file TAPE21 created from the F-coupled calculation in ADF. Reading the starting spin density from the modified TAPE21 file, we can obtain the broken-symmetry state through a single-point energy calculation or geometry optimization.

Typically, the spin Hamiltonian H for transition metal dimers (here Fe1 and Fe2) is expressed via the Heisenberg coupling constant J

$$H = -2J\mathbf{S}_1\cdot\mathbf{S}_2 \tag{1}$$

while for a completely delocalized mixed-valence dimer, a more general spin Hamiltonian is

$$H = -2J_0\mathbf{S}_1\cdot\mathbf{S}_2 \pm B(S_{total} + 1/2) \tag{2}$$

where B is the resonance delocalization parameter. See refs 32 and 33 for detailed discussion of the resonance term, $\pm B(S_{total} + 1/2)$.

---

[25] *ADF 2.3.0*; Theoretical Chemistry, Vrije Universiteit: Vrije, Amsterdam.

[26] Baerends, E. J.; Ellis, D. E.; Ros, P. *Chem. Phys.* **1973**, *2*, 41−59.

[27] te Velde, G.; Baerends, E. J. *J. Comput. Phys.* **1992**, *99*, 84−98.

[28] Guerra, C. F.; Visser, O.; Snijders, J. G.; te Velde, G.; Baerends, E. J. In *Methods and Techniques for Computational Chemistry*; Clementi, E., Corongiu, G., Eds.; STEF: Cagliari, Italy, 1995; p 305.

[29] Vosko, S. H.; Wilk, L.; Nusair, M. *Can. J. Phys.* **1980**, *58*, 1200−1211.

[30] Perdew, J. P.; Chekavry, J. A.; Vosko, S. H.; Jackson, K. A.; Perderson, M. R.; Singh, D. J.; Fioihais, C. *Phys. Rev. B* **1992**, *46*, 6671−6687.

[31] Noodleman, L.; Case, D. A. *Adv. Inorg. Chem.* **1992**, *38*, 423−470.

[32] Mouesca, J.-M.; Chen, J. L.; Noodleman, L.; Bashford, D.; Case, D. A. *J. Am. Chem. Soc.* **1994**, *116*, 11898−11914.

[33] Zhao, X. G.; Richardson, W. H.; Chen, J.-L.; Li, J.; Noodleman, L.; Tsai, H.-L.; Hendrickson, D. N. *Inorg. Chem.* **1997**, *36*, 1198−1217.

[34] Li, J.; Noodleman, L. In *ACS Symposium Series 692: Spectroscopic methods in Bioinorganic Chemistry*; Solomon, E. I., Hodgson, K. O., Eds.; American Chemical Society: Washington, DC, 1998; Chapter 9, pp 179−195.

[35] Case, D. A.; Noodleman, L.; Li, J. In *Metal−Ligand Interactions in Chemistry, Physics and Biology*; Russo, N., Salahub, D. R., Eds.; Kluwer Academic Publishers: Dordrecht, The Netherlands, 2000; pp 19−47.

If the total spin S_{total} is small and B is not large, then the resonance stabilization energy $-B(S_{\text{total}} + 1/2)$ is also small, and the resonance effects can be effectively quenched by environmental effects including solvation, counterions, and vibronic coupling, which produce an asymmetry between the metal sites.[32,33] In this paper, we will ignore this resonance term when calculating the pure-spin ground-state energies. When a Heisenberg Hamiltonian (eq 1) is applicable, the energy difference between F-coupling ($S_{\text{total}} = S_{\max} = S_1 + S_2$) and broken-symmetry (BS) ($S_{\text{total}} = S_{\min} = |S_1 - S_2|$) states can be described by[31−35]

$$E_{\text{F}} - E_{\text{BS}} = -4JS_1S_2 \tag{3}$$

Here, the high-spin energy (E_{F}) is obtained by a single-point energy calculation on the optimized broken-symmetry geometry (which has energy E_{BS}). J is then obtained from eq 3, and the pure-spin ground-state energy E_0 for the particular spin state (S_1, S_2) coupled to $S_{\min}$ according to the broken-symmetry geometry is estimated as

$$E_0 = E_{\text{F}} + JS_{\max}(S_{\max} + 1) - JS_{\min}(S_{\min} + 1) \tag{4}$$

3.3. pK_a Calculations. One cannot compare the absolute energies among the models shown in Figure 3a−d, where the second O atom is present as a H_2O or a OH^- ligand. One has to calculate the pK_a values for the $-H_2O$ ligand (L) forms to compare the relative stability between the L(H_2O) and L(OH^-) active site clusters. The detailed procedure for pK_a calculations can be found from our previous work.[36−38] First, we used a modified version of CHELPG code[40] to fit the point charges from the molecular electrostatic potentials calculated by ADF. Then for solvation energy calculations, we used the MEAD (Macroscopic Electrostatics with Atomic Detail) program suite developed by Bashford, to solve the Poisson−Boltzmann equation using a finite-difference method.[41,42] The solute is represented by a set of atomic charges and Born radii and solvent as a continuous dielectric medium (water with $\epsilon = 80.0$).[36−39] Finally, for the process

$$\text{L(H}_2\text{O)} \rightarrow \text{L(OH}^-) + \text{H}^+ \tag{5}$$

the pK_a value for the L(H_2O) cluster can be calculated by

$$\begin{aligned} 1.37(\text{p}K_a) = \{&E[\text{L(OH}^-)] + E[\text{H}^+] - E[\text{L(H}_2\text{O)}] + E_{\text{corr}}\} + \\ &\{G_{\text{sol}}[\text{L(OH}^-)] - G_{\text{sol}}[\text{L(H}_2\text{O)}]\} - \\ &268.26 = \text{PA} + \Delta G(\text{deproton}) - 268.26 \end{aligned} \tag{6}$$

where $E[\text{L(OH}^-)]$ and $E[\text{L(H}_2\text{O)}]$ represent the gas-phase energies for the active site clusters with ligand $-OH^-$ and $-H_2O$, respectively, $E[\text{H}^+] = 12.6523$ eV is the calculated ionization energy of a spin-restricted H atom obtained from DFT calculation, E_{corr} is a correction term to the proton affinity PA, including zero point energy (ΔZPE $= -7.7$ kcal/mol)[37] and $5/2RT$ work, and -268.26 kcal/mol comes from the sum of the solvation free energy of a proton (-260.5 kcal/mol)[43−45] (using the estimated value of Noyes[45]) and the translation entropy contribution to the gas-phase free energy of a proton ($-T\Delta S_{\text{gas}}(\text{H}^+) = -7.76$ kcal/mol at 298 K and 1 atm pressure).[44]

3.4. Mössbauer Calculations. The detailed methodology for obtaining isomer shift (δ) and quadrupole splitting (QS) properties is outlined in refs 46 and 47. To obtain isomer shifts, all-electron calculations were used to calculate the electron density at the Fe nuclei. For the PW91 potential, the correlation between isomer shifts δ and Fe nuclear densities $\rho(0)$ is given by

$$\delta = \alpha(\rho(0) - 11884.0) + C \tag{7}$$

where $\alpha = -0.664$ and $C = 0.478$ were obtained from a linear correlation between measured isomer shifts and calculated electron densities for a series of 15 dinuclear iron compounds plus 6 polar mononuclear iron complexes.[46]

4. Results and Discussion

4.1. H_2O or OH^-? Bridging or Terminal? To evaluate whether the second oxygen atom in this model is best incorporated as a bridging hydroxide $(OH^-)_{br}$, bridging H_2O $(H_2O)_{br}$, terminal hydroxide $(OH^-)_t$, or terminal H_2O $(H_2O)_t$, we have geometry optimized four kinds of small model clusters. These are shown in Figure 3a−d. To be consistent with known experimental data, we require that these model clusters adopt an Fe(III)−Fe(IV) state and a total cluster spin $S_{\text{total}} = 1/2$ such that the two Fe sites are high-spin AF-coupled,[3] i.e., $\{S_1 = 5/2 \text{ and } S_2 = 2\}$ or $\{S_1 = 2 \text{ and } S_2 = 5/2\}$. This therefore gives rise to 8 possible broken-symmetry optimized gas-phase geometries. Spin projection corrections were then applied to each broken-symmetry energy to obtain ground-state energies. Of the eight states examined, the AF-coupled Fe1(IV)−Fe2(III) state (i.e. $S_1 = 2$, $S_2 = 5/2$) $(OH^-)_{br}$ model has the lowest absolute energy and the shortest Fe−Fe distance (2.738 Å) among all these models. Its broken-symmetry partner, in which the positions of the Fe(III) and Fe(IV) sites are reversed, Fe1(III)−Fe2(IV) state $(OH^-)_{br}$, produces an Fe−Fe distance of 2.776 Å and lies 4.64 kcal/mol higher in energy.

During the geometry optimizations for the Fe1(III)−Fe2(IV) and Fe1(IV)−Fe2(III) states of $(H_2O)_{br}$ (Figure 3b), one of the protons on the introduced water molecule, which originally H-bonds to atom $O_{\delta 1}$ of Asp84, transfers to atom $O_{\delta 1}$, and it therefore appears the bridging water is not stable in this model. The Fe−Fe distances are, in both cases, more than 2.8 Å. pK_a calculations in aqueous solvent for the Fe1(IV)−Fe2(III) $(H_2O)_{br}$ model (which is 1.84 kcal/mol lower in energy than the Fe1(III)−Fe2(IV) $(H_2O)_{br}$ structure) predict its pK_a value to be 0.09, further reinforcing that the

---

(36) Richardson, W. H.; Peng, C.; Bashford, D.; Noodleman, L.; Case, D. A. *Int. J. Quantum Chem*. **1997**, *61*, 207−217.

(37) Li, J.; Fisher, C. L.; Konecny, R.; Bashford, D.; Noodleman, L. *Inorg. Chem*. **1999**, *38*, 929−939.

(38) Huang, H.; Han, W.-G.; Noodleman, L.; Grynszpan, F. *Bioorg. Med. Chem*. **2001**, *9*, 3185−3195.

(39) Han, W.-G.; Lovell, T.; Noodleman, L. *Inorg. Chem*. **2002**, *41*, 205−218.

(40) Breneman, C. M.; Wiberg, K. B. *J. Comput. Chem*. **1990**, *11*, 361−373.

(41) Bashford, D.; Gerwert, K. *J. Mol. Biol*. **1992**, *224*, 473−486.

(42) Bashford, D. In *Scientific Computing in Object-Oriented Parallel Environments*; Lecture Notes in Computer Science; Ishikawa, Y., Oldehoeft, R. R., Reynders, J. V. W., Tholburn, M., Eds.; Springer: Berlin, 1997; Vol. 1343, p 233.

(43) Reiss, H.; Heller, A. *J. Phys. Chem*. **1985**, *89*, 4207.

(44) Tawa, G. J.; Topol, I. A.; Burt, S. K.; Caldwell, R. A.; Rashin, A. A. *J. Chem. Phys*. **1998**, *109*, 4852−4863.

(45) Noyes, R. M. *J. Am. Chem. Soc*. **1962**, *84*, 512−522.

(46) Lovell, T.; Han, W.-G.; Liu, T.; Noodleman, L. *J. Am. Chem. Soc*. **2002**, *124*, 5890−5894.

(47) Liu, T., Lovell, T., Han, W.-G., Noodleman, L. Submitted for publication in *Inorg. Chem*.

Table 1. Geometries (Å), Net Spin Populations, Direct-Calculated Relative Energies (ΔE) (kcal/mol), Heisenberg J Values (cm^{-1}), Spin-Projected Relative Energies (ΔE_0) (kcal/mol), Isomer Shift δ (mm/s), and Quadrupole Splitting (QS) (mm/s) Values for the Large $(OH^-)_{br}$ Model Clusters in Different Spin States[a]

	$S_{max} = 9/2$				$S_{max} = 5/2$			$S_{max} = 3/2$		
		AF (BS)				AF (BS)			AF (BS)	
	F	$S_1 = 5/2$, $S_2 = 2$	$S_1 = 2$, $S_2 = 5/2$	$S_{max} = 7/2$: F	F	$S_1 = 3/2$, $S_2 = 1$	$S_1 = 1$, $S_2 = 3/2$	F	$S_1 = 1/2$, $S_2 = 1$	$S_1 = 1$, $S_2 = 1/2$
geometry										
Fe1−Fe2	2.846	2.804	2.762	2.626	2.586	2.708	2.723	2.561	2.554	2.560
Fe1−O1	2.043	1.894	1.825	1.798	1.787	1.813	1.750	1.787	1.772	1.753
Fe2−O1	1.705	1.708	1.734	1.794	1.796	1.736	1.787	1.786	1.752	1.774
Fe1−O2	2.017	1.971	1.851	1.955	2.060	1.902	1.875	1.914	1.929	1.892
Fe2−O2	2.026	2.074	2.073	1.990	1.905	1.900	1.977	1.903	1.885	1.923
Fe1−$O_{\delta 2}$(Asp84)	1.974	1.983	1.986	1.956	1.949	1.979	1.977	1.970	1.964	1.977
Fe1−$N_{\delta 1}$(His118)	2.199	2.233	2.124	2.219	2.209	2.075	2.114	2.138	2.107	2.138
Fe1−$O_{\epsilon 1}$(Glu238)	2.123	2.127	2.110	2.125	2.079	2.117	2.011	1.963	1.984	1.988
Fe1−$O_{\epsilon 1}$(Glu115)	2.136	2.118	2.102	2.083	2.039	2.108	2.015	1.973	1.977	1.984
Fe2−$O_{\epsilon 2}$(Glu204)	1.940	1.931	1.958	1.935	1.964	1.966	1.965	1.962	1.971	1.959
Fe2−$N_{\delta 1}$(His241)	2.200	2.111	2.153	2.172	2.138	2.099	2.081	2.110	2.133	2.095
Fe2−$O_{\epsilon 2}$(Glu238)	2.073	2.086	2.056	2.089	1.959	1.994	2.091	1.975	1.993	1.980
Fe2−$O_{\epsilon 2}$(Glu115)	2.093	2.095	2.076	2.132	1.973	1.990	2.096	1.966	1.988	1.984
net spin populatn										
Fe1	4.04	−3.74	2.29	2.94	2.94	−2.45	1.63	1.32	−0.64	1.52
Fe2	3.08	2.89	−2.97	3.01	1.41	1.45	−2.58	1.37	1.58	−0.56
O1	0.55	0.20	−0.11	0.17	0.22	0.15	0.09	0.30	0.06	0.03
O2	0.37	−0.26	−0.01	0.29	0.12	0.00	0.04	−0.03	0.03	0.03
ΔE	12.33	5.06	3.36	12.31	4.99	0.55	2.29	0.00	1.32	2.36
J		−161	−333			−439	−355			
ΔE_0	14.30	5.19	1.51	14.28	6.95	0.00	2.22	1.97	3.28	4.33
δ(Fe1)[b]			0.33			0.26		0.30		
δ(Fe2)[b]			0.29			0.36		0.31		
QS(Fe1)[c]			−1.90			1.50		−1.60		
QS(Fe2)[c]			1.70			−1.90		−1.70		

[a] Large $(OH^-)_{br}$ model is shown in Figure 4. F = ferromagnetic, AF= antiferromagnetic, and BS = broken-symmetry. [b] The experimental isomer shift values are 0.56 (Fe^{3+}) and 0.26 (Fe^{4+}) mm/s. [c] The experimental quadrupole splitting values are −0.90 (Fe^{3+}) and −0.60 (Fe^{4+}) mm/s.

$(H_2O)_{br}$ model cluster is less stable energetically than the $(OH^-)_{br}$ structure in the relevant pH range of 6−9.

The optimized $(OH^-)_t$ (Figure 3c) structure for the Fe1(III)−Fe2(IV) state has a long Fe−Fe distance of 2.915 Å and produces a stable terminal OH^- structure. This $(OH^-)_t$ structure is higher in energy by 12.43 kcal/mol than the Fe1(IV)−Fe2(III) $(OH^-)_{br}$ model. Starting from the same $(OH^-)_t$ geometry, the terminal hydroxide switches to the more favored bridging position during the Fe1(IV)−Fe2(III) state geometry optimization.

Optimized Fe−Fe distances exceed 2.9 Å in the $(H_2O)_t$ (Figure 3d) cluster forms for the Fe1(III)−Fe2(IV) and Fe1(IV)−Fe2(III) states. The terminal water molecule is weakly bonded to site Fe2 in both cases with an average distance of 2.3 Å. The pK_a value for the Fe1(IV)−Fe2(III) state $(H_2O)_t$ (which is lower in energy by 3.36 kcal/mol than the Fe1(III)−Fe2(IV) $(H_2O)_t$ state) is calculated to be 1.08. This provides further confirmation that the $(H_2O)_t$ model is also less stable than the $(OH^-)_{br}$ structure.

To conclude this section, assuming the diiron centers are high-spin and AF coupled, for models which contain two bidentate carboxylates and a μ-oxo bridge, an additional oxygen species confers the largest stability on the structure when bridging and in the singly protonated $(OH^-)_{br}$ form for the Fe1(IV)−Fe2(III) state, consistent with the findings of other workers in the field.[19] Though the Fe−Fe distance (2.738 Å) of this structure is the shortest among these calculated models, it is still 0.24 Å longer than the 2.5 Å predicted by EXAFS measurements. The effect that the longer-range protein environment has on the calculated structures and this calculated parameter is now examined. Specifically, we turn to the larger $(OH^-)_{br}$ model to examine if a shorter Fe−Fe distance of around 2.5 Å can be obtained. We also investigate if alternative spin states of the $(OH^-)_{br}$ model lie higher or lower in energy, as well as whether the predicted Mössbauer data from the density functional calculations are consistent with experimental observations.

4.2. Properties of Large Model Cluster $(OH^-)_{br}$ for Different Spin States. Calculated parameters for the possible spin states of the large $(OH^-)_{br}$ model cluster are given in Table 1. Compared to the small model, the Fe−Fe distances in the broken-symmetry optimized ($S_1 = 5/2$, $S_2 = 2$) and ($S_1 = 2$, $S_2 = 5/2$) structures increase from 2.776 and 2.738 Å to 2.804 and 2.762 Å, respectively. The energy of the Fe1(IV)−Fe2(III) ($S_1 = 2$, $S_2 = 5/2$) spin state remains lower than that of the Fe1(III)−Fe2(IV) ($S_1 = 5/2$, $S_2 = 2$) state (the difference after spin decontamination is 4 kcal/mol). These energetic and structural results for the large model are quite consistent with those of the small model cluster.

Mössbauer isomer shift calculations for the optimized ($S_1 = 2$, $S_2 = 5/2$) state are $\delta(Fe1^{4+}) = 0.33$ mm/s and $\delta(Fe2^{3+}) = 0.29$ mm/s. In contrast with the experimental data of $\delta(Fe^{4+}) = 0.26$ mm/s and $\delta(Fe^{3+}) = 0.56$ mm/s, which shows a large difference in Fe site isomer shifts, the calculated δ values for the two iron sites of the ($S_1 = 2$, $S_2 = 5/2$) state are nearly the same. The calculated quadrupole splitting (QS) values are −1.90 and 1.70 mm/s for the two Fe sites. Experimentally, these values are $QS(Fe^{4+}) = -0.60$ mm/s and QS(Fe^{3+}) = −0.90 mm/s. We see also that the calculated QS absolute values for the Fe^{4+} center are larger than the corresponding ones for the Fe^{3+} site and both QS values are comparatively large, which are inconsistent with the experimental data. Given that the calculated isomer shift and quadrupole splittings do not reproduce the experimental parameters very well, as noted earlier, there are a number of ways in which the individual spins of the Fe sites can couple up to $S_{total} = 1/2$. We have also examined other intermediate- and low-spin AF-coupled and F-coupled spin-states to see how their calculated properties compare with the experimental data.

Other possible spin states for the Fe(III)−Fe(IV) cluster are $\{S_A = 3/2$ and $S_B = 2$, with $S_{max} = 7/2\}$, $\{S_A = 3/2$ and $S_B = 1$, with $S_{max} = 5/2\}$, and $\{S_A = 1/2$ and $S_B = 1$, with $S_{max} = 3/2\}$. Geometry optimizations have been performed for all of these F-coupled and broken-symmetry spin-states. The core geometries, net spin populations, directly calculated relative energies (ΔE), and the relative energies (ΔE_0) after spin projection for broken-symmetry states are all given in Table 1.

In a comparison of first the F-coupled spin states with S_{max} decreasing from 9/2 to 7/2, 5/2, and 3/2, the core structures are noted to get more compact and there is a general decrease of the Fe−Fe and of most Fe−ligand distances. This is reasonable as on going from a high-spin $S_{max} = 9/2$ state to intermediate-spin $S_{max} = 3/2$, an increasing number of d-electrons become progressively delocalized in Fe−Fe and Fe−ligand bonds and the intermediate-spin or low-spin ligand fields favor shorter Fe−oxo bonds on average.

The net spins on Fe1 (2.94) and Fe2 (3.01) of the optimized F-coupled $S_{max} = 7/2$ structure are calculated to be nearly equal. Therefore, one cannot distinguish the Fe(III) and Fe(IV) sites in this state. Using the $S_{max} = 7/2$ spin density as a starting point, we were unable to successfully locate the $\{S_1 = 3/2, S_2 = 2\}$ and $\{S_1 = 2, S_2 = 3/2\}$ broken-symmetry states in our calculations. Instead, the broken-symmetry geometry optimizations converged to the $\{S_1 = 3/2, S_2 = 1\}$ and $\{S_1 = 1, S_2 = 3/2\}$ states.

Starting from the $S_{max} = 9/2$ and $S_{max} = 5/2$ states, the spin flipped broken-symmetry derived states lie lower in energy. However, the F-coupled $S_{max} = 3/2$ state has the lowest directly calculated energy among all the different spin states studied here, and this state also displays a very short Fe−Fe distance (2.561 Å), which is close to the value of 2.5 Å predicted by EXAFS. The two broken-symmetry states of $\{S_1 = 1/2, S_2 = 1\}$ and $\{S_1 = 1, S_2 = 1/2\}$ also give very short Fe−Fe distances, but these states lie at higher energy (higher than their corresponding high-spin state with $S_{total} = 3/2$). The net-spin values given in Table 1 for these states are very similar to the net spin densities noted in the model for X obtained by Siegbahn using a different exchange-correlation potential (B3LYP),[19] which probably is the $\{S_1 = 1/2, S_2 = 1\}$ broken-symmetry state.

After application of spin-projection corrections, there is a distinct reordering in the energies of the F-coupled and AF-coupled states. The AF-coupled state, $\{S_1 = 3/2, S_2 = 1\}$, now lies lowest in energy. The AF-coupled $\{S_1 = 2, S_2 = 5/2\}$ state lies only slightly higher in energy at +1.51 kcal/mol, followed by the F-coupled $S = 3/2$ state now at +1.97 kcal/mol. We see also from Table 1 that, for these three lowest lying states, a number of Fe−N (His118, His241) and Fe−O (bridging carboxylate, Glu115, Glu238) distances become shorter as the site spins decrease. Since protein constraints can affect first shell metal−ligand distances, and all these energies are quite close, protein control of the ground electronic state (particularly the site spin state) is quite feasible both here and more generally.

Mössbauer property calculations were then performed on the lowest-energy structures with the AF-coupled $\{S_1 = 3/2, S_2 = 1\}$ state, and the calculated isomer shift and quadrupole splitting values are $\delta(\mathrm{Fe1}^{3+}) = 0.26$, $\delta(\mathrm{Fe2}^{4+}) = 0.36$, QS($\mathrm{Fe1}^{3+}$) = 1.50, and QS($\mathrm{Fe2}^{4+}$) = −1.90 mm/s. Again, the calculated δ and QS absolute values for the Fe^{4+} center are larger than the corresponding ones for the Fe^{3+} site, which is not in agreement with the experimental observation. Calculated absolute values of quadrupole splittings are also much larger than the corresponding experimental ones. Mössbauer properties were also calculated for the F-coupled $S = 3/2$ state (which is the third lowest energy structure). Its isomer shift and quadrupole splitting values are δ(Fe1) = 0.30, δ(Fe2) = 0.31, QS(Fe1) = −1.60, and QS(Fe2) = −1.70 mm/s. We see both the isomer shift and quadrupole splitting values for the two iron sites are very close to each other. As might be expected for a delocalized mixed-valence state, one cannot distinguish the Fe(III) and Fe(IV) sites from these δ and QS data.

Finally, it has been observed experimentally that there is significant spin delocalization on to the oxygen ligand(s).[3] The net-spin analysis shown here in Table 1 for the spin states we have described reveals that, with the exception of the $\{S_1 = 5/2, S_2 = 2\}$ state, the net spin associated with atom O2 (in bridging hydroxyl) is nearly zero for the majority of the AF-coupled spin states. Atom O1 (O_μ) shows some associated spin density for most of the calculated states, while, for all AF-coupled states, net spin values on other ligated oxygen atoms from carboxylates are less than 0.1 and are not listed in Table 1.

5. Conclusions

Several possible core structures (see Figure 2) for RNR intermediate X have been suggested on the basis of recent experimental observations.[15−18] In these models, it has been proposed that two carboxylates from Glu115 and Glu238 are monodentate or bidentate binding to the diiron centers and that there are two oxygen atoms derived initially from O_2. One oxygen is present as a μ-oxo bridge, and the other, as terminal or bridging H_2O or OH^-.[17] In this paper, using spin-unrestricted density functional theory with broken-symmetry and spin-projection methodology, we have studied the geometries, spin states, spin densities, and Mössbauer properties for one of these model diiron clusters (Figures 2c, 3, and 4).

Our model contains two bidentate carboxylate groups and a μ-oxo bridge. Calculations on smaller core structure model clusters (Figure 3) show that introduction of a second oxygen species is most energetically favored as a bridging hydroxide (Figure 3a).

When the most favorable model is surrounded by second- and third-shell ligands similar to that found in the protein environment (Figure 4), the lowest energy structure displays both an Fe−Fe distance of 2.708 Å and an AF-coupled configuration of $\{S_1 = 3/2, S_2 = 1\}$. However, experimentally, it is clear that X displays a high-spin AF-coupled $S_{\text{total}} = 1/2$ ground state (i.e. $S_A = 5/2$, $S_B = 2$) with significant spin delocalization onto the oxygen ligand(s),[3] and EXAFS data analysis indicates a short Fe−Fe distance of about 2.5 Å. Mössbauer property calculations for three lowest energy structures with different spin states, including one resembling the experimentally observed $S_{\text{total}} = 1/2$ ground state where the Fe sites retain a high-spin configuration, produce similar isomer shift and quadrupole splitting values for Fe1 and Fe2 sites. This differs significantly from the experimental situation in which the two iron sites can be distinguished on the basis of their different isomer shift and quadrupole splitting parameters. The calculated absolute quadrupole splitting values are all considerably larger than the observed ones. For the AF-coupled $\{S_1 = 2, S_2 = 5/2\}$ and $\{S_1 = 3/2, S_2 = 1\}$ states, the calculated isomer shift and quadrupole splitting data for the Fe(IV) center are larger than the corresponding ones for the Fe(III) site, which is also inconsistent with the experimental observations.

Very recently, we have studied another similar diiron (Fe(IV)−Fe(IV)) cluster model for the intermediate Q of the methane monooxygenase (MMO).[46] In that model for Q, high-spin iron sites were calculated to have lowest energy. There are several possible reasons our models for X and Q differ in the nature of the ground state obtained from the broken-symmetry calculations. (1) Different models were used to approximate Q and X, and the full effects of the differing bridging ligands, oxo versus hydroxo, on the nature of the ground state and Mössbauer parameters are yet to be fully understood. (2) One more electron in X compared to Q results in a III,IV system rather than IV,IV. (3) There are differences in the second and third shell environments in the models of Q and X—in particular, the His-Asp-Arg motif is lost for one of the iron sites in X compared to Q. Such protein differences or constraints can affect metal−ligand distances such that the spin ground state of a particular iron site is sensitive to the local second shell environment. Also, iron−oxygen distances become shorter for low-spin or intermediate-spin iron sites. (4) The result of the lowering of the intermediate- and low-spin states is that all states in the current model of X are much closer than all the states in Q. (5) The iron sites in Q are calculated to be 5 coordinate; in the X model they are six coordinate. The latter coordination favors intermediate and low spin for the iron sites while, in general, more open structures, as in Q, favor high-spin sites. (6) DFT is not perfect in distinguishing very close lying spin states. Some or all of these factors in combination will affect the ordering of the high-spin versus intermediate-spin versus low-spin states in X relative to those calculated for Q.

According to the present calculations, although the model diiron cluster displays structural elements consistent with current experimental data, the contrast between the calculated and experimental properties, particularly the Mössbauer data, implies that the model cluster we have examined herein is unlikely to be that of RNR intermediate X. More open structures than those shown in the Figures 3 and 4 with additional monodentate rather than bidentate carboxylate bridging from Glu238 and altered solvent coordination can alter Mössbauer isomer shifts, quadrupole splittings, and structures.[47,48] A number of these structures are currently under investigation in our laboratory.

The model we studied here, which contains two bidentate carboxylate bridges, a μ-O and a μ-OH bridge, was calculated to have the distance of Fe−Fe > 2.7 Å for AF-coupled high-spin and intermediate-spin states. It is difficult to envision that alternative structures to the present model would yield structures with Fe−Fe distance shorter than 2.7 Å. In that context, it is also difficult to see how the observed Mössbauer parameters can be compatible with the very short Fe−Fe distance (2.5 Å) from EXAFS.

In the future, it would be valuable also to investigate radiolytically more oxidized forms of RNR (compared to RNR_{ox}) and radiolytically reduced intermediate Q in MMOH or related synthetic complexes, to see if some systems have structures and Mössbauer properties similar to those we have found.

Acknowledgment. We thank the NIH for financial support (Grant GM43278 to L.N.). The generous support of computer time on the SGI clusters of the Scripps Research Institute is gratefully acknowledged.

IC020465L

---

(48) Han, W.-G., Lovell, T., Liu, T., Noodleman, L. Submitted for publication in *Inorg. Chem*.